

2017-09

The limitations of hibonite as a single-mineral oxybarometer for early solar system processes

Berry, AJ

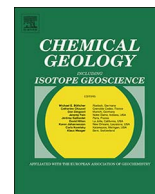
<http://hdl.handle.net/10026.1/9833>

10.1016/j.chemgeo.2017.03.031

Chemical Geology

Elsevier BV

All content in PEARL is protected by copyright law. Author manuscripts are made available in accordance with publisher policies. Please cite only the published version using the details provided on the item record or document. In the absence of an open licence (e.g. Creative Commons), permissions for further reuse of content should be sought from the publisher or author.



The limitations of hibonite as a single-mineral oxybarometer for early solar system processes



Andrew J. Berry^{a,b,c,*}, Paul F. Schofield^c, Antonina N. Kravtsova^d, Laura A. Miller^b,
Natasha R. Stephen^e, Andrew M. Walker^f, Alexander V. Soldatov^d, Trevor R. Ireland^a, K. Geraki^g,
J. Fred W. Mosselmans^g

^a Research School of Earth Sciences, Australian National University, Canberra, ACT 2601, Australia

^b Department of Earth Science and Engineering, Imperial College London, South Kensington, SW7 2AZ, UK

^c Department of Earth Sciences, Natural History Museum, Cromwell Road, London SW7 5BD, UK

^d International Research Centre "Smart Materials", Southern Federal University, Sorge 5, Rostov-on-Don 344090, Russia

^e Plymouth Electron Microscopy Centre, Plymouth University, Drake Circus, Plymouth PL4 8AA, UK

^f School of Earth and Environment, University of Leeds, Leeds LS2 9JT, UK

^g Diamond Light Source, Harwell Science and Innovation Campus, Didcot OX11 0DE, UK

ARTICLE INFO

Keywords:

Hibonite

Calcium hexaluminate

CA6

CAI

Oxybarometry

Solar nebula

Crystal chemistry

Oxygen fugacity

XANES

FDMNES

ABSTRACT

The relationships between the composition of hibonite with the general formula $\text{CaAl}_{12-2x-y}\text{Mg}_x\text{Ti}^{4+}_x\text{Ti}^{3+}_y\text{O}_{19}$, the oxidation state of Ti ($\text{Ti}^{3+}/\Sigma\text{Ti}$, where $\Sigma\text{Ti} = \text{Ti}^{3+} + \text{Ti}^{4+}$), and oxygen fugacity ($f\text{O}_2$) were investigated experimentally. It was found that hibonite can be synthesised with a range of $\text{Ti}^{3+}/\Sigma\text{Ti}$ values at constant $f\text{O}_2$ and with a constant $\text{Ti}^{3+}/\Sigma\text{Ti}$ value for a range of $f\text{O}_2$ s. It was also found that if hibonite with the formula $\text{CaAl}_{12-2x-y}\text{Ti}^{3+}_y\text{O}_{19}$ ($\text{Ti}^{3+}/\Sigma\text{Ti} = 1$) is equilibrated with a melt of CAI composition at $f\text{O}_2$ s below the iron-wüstite buffer then the resulting hibonite contained Mg, with Mg per formula unit (pfu) ~ 0.8 Ti pfu, and $\text{Ti}^{3+}/\Sigma\text{Ti} \sim 0.2$, irrespective of the $f\text{O}_2$. These results suggest that the availability of Mg, rather than $f\text{O}_2$, is the key factor that determines $\text{Ti}^{3+}/\Sigma\text{Ti}$ of hibonite. The structures of synthetic samples of hibonite with the general formula $\text{CaAl}_{12-2x}\text{Mg}_x\text{Ti}^{4+}_x\text{O}_{19}$, where $0 \leq x < 1$, were determined by Rietveld refinement of X-ray powder diffraction data. The predominant site occupied by Ti^{4+} was found to change from M2 to M4 with increasing Ti content. The range of Ti concentrations over which the site occupancy changed corresponds to that observed in meteoritic hibonite. This change in the Ti^{4+} site produces changes in the Ti K-edge XANES spectra, particularly in the intensity of the pre-edge feature, for constant $\text{Ti}^{3+}/\Sigma\text{Ti}$. The observed dependence of the pre-edge on the Ti^{4+} site was reproduced by *ab initio* simulations of the XANES spectra. The XANES spectra of natural hibonite with variable Ti content from the Murchison carbonaceous chondrite closely match the spectra of the synthetic samples with similar Ti contents. These differences in the spectra of meteoritic hibonite could be misinterpreted as being due to changes in $\text{Ti}^{3+}/\Sigma\text{Ti}$, but are instead due to differences in ΣTi , which relate to the petrogenetic history. Crystal chemistry exerts a first order control on the Ti site occupancy and $\text{Ti}^{3+}/\Sigma\text{Ti}$ value of hibonite. As a result, no simple relationship between $\text{Ti}^{3+}/\Sigma\text{Ti}$ and $f\text{O}_2$ should be expected. It is unlikely that hibonite will be useful as an oxybarometer for solar processes without $\text{Ti}^{3+}/\Sigma\text{Ti}$ standards that are compositionally matched to the unknown.

1. Introduction

Hibonite ($\text{CaAl}_{12}\text{O}_{19}$) is the second mineral, after corundum, to condense from a gas of solar composition (Kornacki and Fegley, 1986; Yoneda and Grossman, 1995; Lodders, 2003). It incorporates varying amounts of Ti as both Ti^{3+} and Ti^{4+} . Ti^{3+} substitutes directly for Al^{3+} whereas Ti^{4+} undergoes a charge coupled substitution with Mg^{2+}

($\text{Ti}^{4+} + \text{Mg}^{2+} = 2\text{Al}^{3+}$). A general formula for Ti-bearing hibonite is $\text{CaAl}_{12-2x-y}\text{Mg}_x\text{Ti}^{4+}_x\text{Ti}^{3+}_y\text{O}_{19}$. There are five Al sites in hibonite (M1–M5) and their multiplicity and coordination numbers are given by $^{[12]}\text{Ca}^{[6]}\text{M1}^{[5]}\text{M2}^{[4]}\text{M3}_2^{[6]}\text{M4}_2^{[6]}\text{M5}_6\text{O}_{19}$ (where coordination numbers are superscripted in square brackets and the multiplicity of the site is subscripted). It has been shown recently by neutron powder diffraction (NPD) of synthetic hibonite, and density functional theory (DFT),

* Corresponding author at: Research School of Earth Sciences, Australian National University, Canberra, ACT 2601, Australia.

E-mail address: andrew.berry@anu.edu.au (A.J. Berry).

that Ti^{3+} occupies adjacent face-sharing octahedral M4 sites due to a stabilising Ti–Ti interaction, Ti^{4+} occupies both the M2 and M4 sites (~ 1.5 at 1400°C) with the occupancy of M4 again stabilised by a Ti–Ti interaction, and Mg occupies the tetrahedral M3 site and Mg–Ti interactions are not important (Doyle et al., 2014). These site occupancies are broadly consistent with results obtained by single-crystal X-ray diffraction (Giannini et al., 2014). In dilute systems, where Ti is present as isolated cations, Ti^{3+} is predicted to occupy M2, Ti^{4+} the M2 site, and Mg^{2+} the M3 site (Doyle et al., 2014).

It has been proposed that the ratio of Ti^{3+} to Ti^{4+} in hibonite, given as $\text{Ti}^{3+}/\Sigma\text{Ti}$ where $\Sigma\text{Ti} = \text{Ti}^{3+} + \text{Ti}^{4+}$, may record the oxygen fugacity ($f\text{O}_2$) at the time of crystallisation/condensation from the solar nebula or of a later reprocessing event (Ihinger and Stolper, 1986; Beckett et al., 1988). The presence of Ti^{3+} results in a blue colour that is often considered to be diagnostic of meteoritic hibonite and the intensity of the absorption band that gives rise to this colour has been used to provide constraints on the $f\text{O}_2$ at which crystals equilibrated (Ihinger and Stolper, 1986). $\text{Ti}^{3+}/\Sigma\text{Ti}$ in hibonite has been quantified from the intensity of the electron spin resonance (ESR) signal arising from the unpaired electron in Ti^{3+} , and values of ~ 0.2 were obtained for samples from the Murchison carbonaceous chondrite (Beckett et al., 1988), however, relating $\text{Ti}^{3+}/\Sigma\text{Ti}$ to $f\text{O}_2$ was compromised by the uncertain Ti site occupancies. These attempts to determine $f\text{O}_2$ using hibonite gave values that were either poorly constrained or significantly more oxidised than expected.

X-ray absorption near edge structure (XANES) spectroscopy is a technique that allows oxidation state ratios to be determined with micron spatial resolution and a precision of $\pm 1\%$ (absolute) (e.g. Berry et al., 2008, 2010). It has been used to determine the Ti site and oxidation state in minerals (e.g. Berry et al., 2007; Simon et al., 2007; Tailby et al., 2011). Spatially-resolved soft X-ray spectroscopies such as X-ray photo-emission electron microscopy (XPEEM) and scanning transmission X-ray microscopy (STXM) also have the potential to accurately quantify oxidation states and image their distribution (Schofield et al., 2014). Integral to correctly interpreting the results of any spectroscopic technique in terms of $\text{Ti}^{3+}/\Sigma\text{Ti}$ is an understanding of the crystal chemistry, since cations with the same oxidation state at different crystallographic sites can give different spectra.

Here we present the results of three sets of experiments on the roles of crystal chemistry and $f\text{O}_2$ on the $\text{Ti}^{3+}/\Sigma\text{Ti}$ value of hibonite and hence the suitability of hibonite as a single mineral oxybarometer. Firstly, the site occupied by Ti^{4+} in hibonite with the general formula $\text{CaAl}_{12-2x}\text{Mg}_x\text{Ti}^{4+}_x\text{O}_{19}$ (i.e. $\text{Ti}^{3+}/\Sigma\text{Ti} = 0$) was determined for variable ΣTi by Rietveld refinement of X-ray diffraction (XRD) data. XANES spectra of these samples were compared to those predicted for Ti^{4+} at different defect sites and those of meteoritic hibonite. Secondly, hibonite with the general formula $\text{CaAl}_{12-y}\text{Ti}^{3+}_y\text{O}_{19}$ (i.e. $\text{Ti}^{3+}/\Sigma\text{Ti} = 1$) was equilibrated with a melt of calcium–aluminium inclusion (CAI) composition, at different $f\text{O}_2$ s. These experiments were designed to simulate possible reactions between early-formed hibonite and further condensate or melt in the solar nebula. Thirdly, oxides corresponding to hibonite with the general formula $\text{CaAl}_{12-2x-y}\text{Mg}_x\text{Ti}^{4+}_x\text{Ti}^{3+}_y\text{O}_{19}$ were equilibrated at 1400°C to determine the $f\text{O}_2$ range over which hibonite with a particular $\text{Ti}^{3+}/\Sigma\text{Ti}$ value is stable.

2. Experimental

Samples are identified by reference to their Ti per formula unit (pfu) and $\text{Ti}^{3+}/\Sigma\text{Ti}$ ratios using the notation (Ti pfu, $\text{Ti}^{3+}/\Sigma\text{Ti}$). For example, the sample (1.0, 1.0) will have 1.0 Ti pfu and all the Ti will be Ti^{3+} giving a chemical formula of $\text{CaAl}_{11.0}\text{Ti}_{1.0}\text{O}_{19}$. The sample (1.0, 0.0) will have 1.0 Ti^{4+} pfu (and 1.0 Mg^{2+} pfu) giving a chemical formula of $\text{CaAl}_{10.0}\text{Ti}_{1.0}\text{Mg}_{1.0}\text{O}_{19}$.

To investigate the effect of different amounts of Ti^{4+} on the structure of hibonite, samples with the compositions (0.0, 0.0), (0.1, 0.0), (0.2, 0.0), (0.3, 0.0) and (0.4, 0.0) (i.e. the general formula CaAl_{12-2x}

$_{2x}\text{Mg}_x\text{Ti}^{4+}_x\text{O}_{19}$) were prepared from stoichiometric mixtures of CaCO_3 , Al_2O_3 , $(\text{NH}_4)_2\text{TiO}(\text{C}_2\text{O}_4)_2 \cdot n\text{H}_2\text{O}$ ($n \sim 1$; ammonium titanium oxalate or ammonium bis(oxalato)oxotitanate(IV) hydrate, CAS 10580-03-7) and $\text{Mg}(\text{NO}_3)_2 \cdot n\text{H}_2\text{O}$ ($n \sim 6$). $(\text{NH}_4)_2\text{TiO}(\text{C}_2\text{O}_4)_2 \cdot n\text{H}_2\text{O}$ and $\text{Mg}(\text{NO}_3)_2 \cdot n\text{H}_2\text{O}$ were standardised by firing at 1000°C to determine the yields of TiO_2 and MgO , respectively. $(\text{NH}_4)_2\text{TiO}(\text{C}_2\text{O}_4)_2 \cdot n\text{H}_2\text{O}$ is soluble in water, and $\text{Mg}(\text{NO}_3)_2 \cdot n\text{H}_2\text{O}$ is soluble in both water and acetone, and solutions of each were added separately to a mixture of CaCO_3 and Al_2O_3 and stirred until the solvent evaporated. The addition of Ti and Mg in solution ensures that these elements, which are present at low concentrations, are homogeneously distributed in the resulting mix. The mix was pressed into a pellet and heated at 1400°C (the incongruent melting point of $\text{CaAl}_{12}\text{O}_{19}$ is 1852°C ; Jerebtsov and Mikhailov, 2001) in an atmosphere of CO_2 (corresponding to an $f\text{O}_2$ of $+6.7$ log units relative to the iron–wüstite, IW, buffer) for 24 h, cooled to 600°C , reground, and re-heated at 1400°C for a further 24 h. Samples of (0.44, 0.0), (0.98, 0.0), and (0.20, 1.0) were prepared previously from mixtures of CaCO_3 , Al_2O_3 , TiO_2 , and MgO (Doyle et al., 2014).

To investigate changes in hibonite composition due to equilibration with a melt, samples of Ti^{3+} hibonite were prepared from mixtures of CaCO_3 , Al_2O_3 , and $(\text{NH}_4)_2\text{TiO}(\text{C}_2\text{O}_4)_2 \cdot n\text{H}_2\text{O}$ ((0.15, 1.0) and (0.25, 1.0)), or CaCO_3 , Al_2O_3 , and TiO_2 ((0.30, 1.0)), in equilibrium with graphite and CO at 1400°C , powdered, and mixed with either composition Hib2Ti5 of Beckett and Stolper (1994) (SiO_2 21.18, TiO_2 4.85, MgO 3.35, Al_2O_3 44.53, CaO 26.55, all as wt%, called A, prepared from oxides and CaCO_3) or a modified version of this composition without TiO_2 (called B), in the proportions 40% hibonite, 60% Hib2Ti5 (by wt). The composition Hib2Ti5 was chosen because it gives melt and hibonite at $\sim 1450^\circ\text{C}$ over an $f\text{O}_2$ range from at least IW–3.3 to IW + 6.6. The resulting powders were mixed with polyethylene oxide and water to form a paste, which was mounted on wire loops, and equilibrated at 1450°C and values of $\log f\text{O}_2$ corresponding to IW–0.3, –1.3, –2.3, –3.3, and –4.3. The loops were made of Pt for IW–0.3, –1.3, and –2.3, and Re for IW–3.3 and –4.3. The $f\text{O}_2$ was controlled using mixtures of CO and CO_2 . Powders were also pressed into a pellet and equilibrated with graphite and CO (IW–6.3). After at least 24 h the samples were quenched in water (see Burnham et al., 2015 for further experimental details).

To investigate the $f\text{O}_2$ stability range of hibonite, mixtures of oxides corresponding to the hibonite compositions (0.98, 0.0), (0.62, 0.6), and (0.33, 1.0) were pressed into pellets and heated at 1400°C and values of $\log f\text{O}_2$ equal to IW–6.3, –2.3, –0.3, +2.3, +4.3, +7.3, as described above, for ~ 24 h. All samples were held in Pt wire baskets except for those at IW–6.3, which were in graphite.

Portions of all samples were mounted in epoxy resin and polished for imaging and XANES spectroscopy. Portions were also powdered for quantitative phase analysis and structural characterisation using XRD. Samples of hibonite from the Murchison carbonaceous chondrite (Ireland, 1988, 1990) were presented as crystal fragments pressed into gold (Ireland et al., 1992).

High-spatial-resolution back-scattered electron (BSE) images and elemental maps were acquired using a JEOL 7001 FE-SEM, operating at 15 kV and a working distance of 10 mm, with AZtec software (Oxford Instruments). Compositions were determined using a Cameca SX-100 electron probe (EPMA), operating at 15 kV and 20 nA, with LTAP (for Si, Mg and Al) and PET (for Ca and Ti) crystals. Wollastonite (for Si and Ca), forsterite (Mg), corundum (Al) and synthetic MnTiO_3 (Ti) were used as standards and the detection limits (wt%) were 0.02 for Si, Mg and Al, 0.05 for Ca, and 0.04 for Ti.

XRD patterns were collected using a $\theta/2\theta$ PANalytical X'Pert Pro $\alpha 1$ X-ray diffractometer with an X'celerator real-time strip-detector that has an active detector length of 2.122° . Data for quantitative phase analysis (QPA) and structural characterisation were collected using Cu K α and Cu K α_1 radiation, respectively. For QPA, data were collected from powdered samples on kapton film, in transmission geometry,

Table 1

Lattice parameters and Mg and Ti site occupancies (as fractions of 1) of synthetic hibonite with $\text{Ti}^{3+}/\Sigma\text{Ti} = 0$ determined by Rietveld refinement of XRD data. Ti^{4+} (M4) was calculated assuming that $\text{Ti}^{4+} \text{ pfu} = \text{Mg}^{2+} \text{ pfu}$.

Sample	<i>a</i> (Å)	<i>c</i> (Å)	Volume (Å ³)	Mg (M3)	Ti ⁴⁺ (M2 ^a)	Ti ⁴⁺ (M4)	Ti ⁴⁺ (M2/M4)
(0.0, 0.0)	5.55769 (2)	21.8958 (2)	585.708 (4)	–	–	–	–
(0.10, 0.0)	5.56305 (2)	21.9095 (1)	587.204 (3)	0.05	0.035 (5)	0.015 (5)	2.33 (84)
(0.20, 0.0)	5.56790 (2)	21.92436 (9)	588.627 (3)	0.10	0.050 (5)	0.050 (5)	1.00 (14)
(0.30, 0.0)	5.57443 (2)	21.9430 (1)	590.512 (3)	0.15	0.065 (5)	0.085 (5)	0.76 (7)
(0.40, 0.0)	5.58060 (2)	21.9653 (1)	592.419 (3)	0.20	0.075 (5)	0.125 (5)	0.60 (5)
(0.44, 0.0)	5.58874 (7)	21.9986 (6)	595.05 (1)	0.21	0.05 (1)	0.16 (2)	0.31 (7)
(0.98, 0.0)	5.6065 (1)	22.0700 (5)	600.79 (3)	0.48	0.136 (7)	0.34 (1)	0.40 (2)

^a Site is half occupied.

between 5 and 97 °2θ using a step size of 0.017 ° and a scan rate of 0.001 °s^{−1}, resulting in total scan times of ~23 h. For structural characterisation, data were collected from powdered samples packed into a top-loaded deep-well sample holder, in reflection geometry, between 5 and 125 °2θ using a step size of 0.017 ° and a scan rate of 0.0056 °s^{−1}, resulting in total scan times of ~6 h. The samples were spun in the plane of the sample surface during data collection in both geometries. The resulting patterns were analysed by Rietveld refinement within the GSAS (General Structure Analysis System) code of Larson and Von Dreele (1994) interfaced with EXPGUI (Toby, 2001). For both the QPA and crystal structure refinements the starting models used data for Ti-bearing hibonite from Doyle et al. (2014). For the QPA, peak profiles (type 2) were modelled using the model-dependent Le Bail method and the backgrounds using a six-term power series function. Phases were identified by pattern matching using the JCPDS database

of the International Centre for Diffraction Data. Phase proportions were quantified using the Rietveld method in which the scale factor, phase fractions and cell parameters were refined simultaneously. The unit cell parameters were allowed to vary but no attempt was made to iterate the site occupancies. The refinements were constrained to maintain chemical mass balance such that the final chemistry closely matched the composition of the original oxide mix. The final refinement sequences included a six-term, spherical-harmonic preferred orientation parameter for hibonite. For the crystal structure refinements, peak profiles (type 2) were also modelled using the Le Bail method but the backgrounds used a four-term power series function. The structural parameters of additional phases (if any) were added, the diffraction patterns were scaled, and then all phases were refined simultaneously. For hibonite, the unit-cell parameters were refined first, followed by the atomic coordinates and atomic displacement parameters (ADP). The Ti

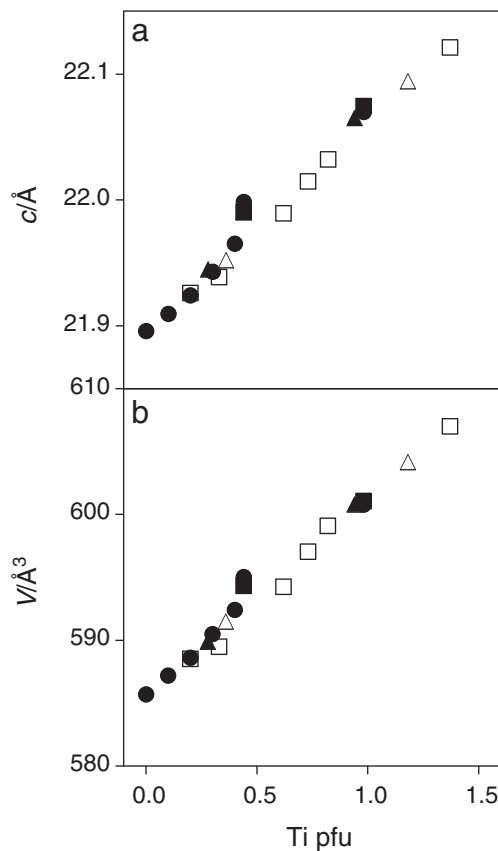


Fig. 1. (a) *c* lattice parameter and (b) *V*, unit cell volume, as a function of Ti pfu, determined for synthetic hibonite ($\text{CaAl}_{12-2x}\text{Mg}_x\text{Ti}^{4+}_x\text{O}_{19}$) in this study (circles), and from Doyle et al., 2014 (squares) and Giannini et al., 2014 (triangles). Samples with $\text{Ti}^{3+}/\Sigma\text{Ti} = 0$ are denoted by solid symbols and those containing Ti^{3+} by open symbols. Error bars are smaller than the symbols.

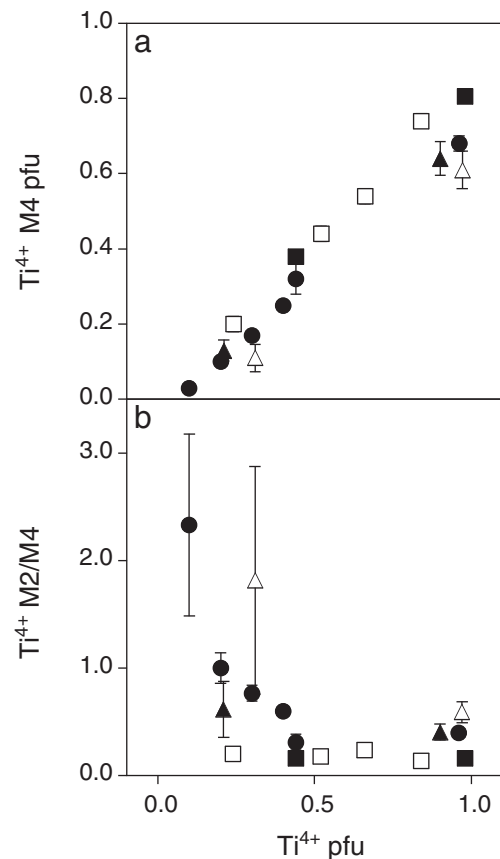


Fig. 2. Ti^{4+} on (a) M4 in pfu and (b) M2/M4, as a function of Ti^{4+} pfu for synthetic hibonite in this study (circles), Doyle et al., 2014 (squares), and Giannini et al., 2014 (triangles). Samples with $\text{Ti}^{3+}/\Sigma\text{Ti} = 0$ are denoted by solid symbols and those containing Ti^{3+} by open symbols. The error bars are smaller than the symbols except where shown.

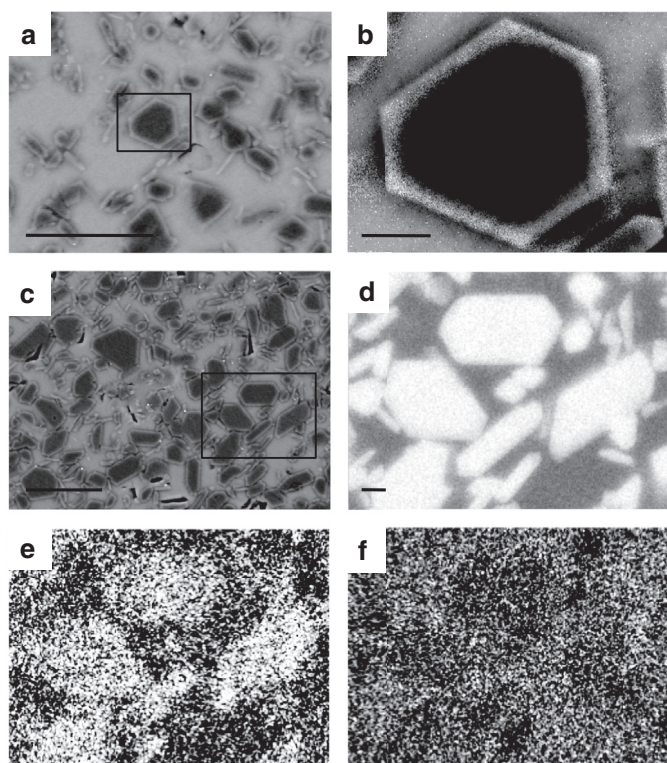


Fig. 3. FE-SEM BSE images of hibonite crystals (dark) in melt of CAI composition produced by equilibrating (a) (0.15, 1.0) in melt A at IW = 4.3 and (c) (0.15, 1.0) in melt B at IW = 3.3. (b) Ti, Ca, and Al composite elemental map, highlighting the distribution of Ti in a crystal of hibonite, of the area indicated by the box in (a). Elemental maps corresponding to the area indicated by the box in (c) are shown for (d) Al, (e) Ti, and (f) Mg. The scale bars in (a) and (c) are 20 μm and those in (b) and (d) are 2 μm .

(and Mg by stoichiometry) site occupancies were fixed during the least squares refinements and manually iterated between refinement cycles.

Titanium K-edge XANES spectra were recorded at I18 of Diamond Light Source (Mosselmans et al., 2009). The excitation energy was selected using a Si(111) monochromator and calibrated by defining the first derivative peak of a Ti foil spectrum to be at 4966.4 eV. The energy resolution at the Ti K-edge was 0.70 eV, which when coupled with the Ti K α core-hole width of 0.94 eV resulted in a spectral resolution of 1.2 eV. High-energy harmonics were removed by Rh coated KB mirrors that were used to focus the beam to $\sim 3 \times 3 \mu\text{m}$. The penetration depth of Ti K-edge X-rays (absorption length) in $\text{CaAl}_{12}\text{O}_{19}$ is $\sim 17 \mu\text{m}$. Fluorescence was detected using either a nine-element Ge or a four-element Si drift (Vortex) detector and the distance between the detector and sample was adjusted to ensure that the total incoming count rate was within the linear range of the signal processing electronics. Samples were mounted at 45° to both the incident beam and the detector. Spectra were recorded from 4950 to 5200 eV with a step size of 0.5 eV for the baseline (4950–4960 eV), 0.1 eV for the pre-edge (4960–4975), 0.2 eV for the edge (4975–5015) and 2.5 eV above the edge. The total spectral acquisition time was ~ 20 min. The Ti K α fluorescence intensity was dead-time corrected, normalised to the intensity of the incident beam, and the resulting spectra compared after subtraction of a constant baseline and normalisation to the average intensity above 5145 eV. For the synthetic samples spectra were recorded from a number of points. Spectra of meteoritic crystals were recorded for random orientations.

The Ti K-edge XANES spectra of Ti^{3+} and Ti^{4+} occupying various sites in hibonite were simulated using the full-potential finite difference method to solve the Schrödinger equation in real space while accounting for the core hole created by the electronic transition. The simulations made use of the FDMNES program (Joly, 2001; Bunau and Joly, 2009) and the Hedin-Lundqvist exchange-correlation potential. Atomic

geometries corresponding to the different defects used in the simulations were taken from the DFT calculations described in Doyle et al. (2014). Specifically, spectra were calculated for isolated Ti^{3+} on M2, isolated Ti^{4+} on either M2 or M4, and clusters of either two Ti^{3+} or two Ti^{4+} on adjacent face-sharing M4 sites. Ti^{4+} was charge balanced by Mg^{2+} on M3. These geometries correspond to models $\text{Ti}_{\text{Al}(2)}^\times$, $\{\text{Ti}_{\text{Al}(2)}^\times \text{Mg}_{\text{Al}(3)}^\times\}_b$, $\{\text{Ti}_{\text{Al}(4)}^\times \text{Mg}_{\text{Al}(3)}^\times\}$, $\{\text{Ti}_{\text{Al}(4)}^\times \text{Ti}_{\text{Al}(4)}^\times\}$ and $\{\text{Ti}_{\text{Al}(4)}^\times \text{Ti}_{\text{Al}(4)}^\times \text{Mg}_{\text{Al}(3)}^\times \text{Mg}_{\text{Al}(3)}^\times\}$, respectively, in Tables 5 and 6 of Doyle et al. (2014). For each model a spherical atomic cluster of radius 5.6 Å around the central Ti cation was extracted from the periodic model (previously subjected to geometry optimisation using DFT) and this finite cluster was used for the simulation of the XANES spectra. The calculated spectra were arbitrarily shifted in energy in order to align them with the experimental spectra.

3. Results

The $\text{CaAl}_{12-2x}\text{Mg}_x\text{Ti}^{4+}_x\text{O}_{19}$ samples (i.e. those prepared at 1400 °C and IW + 6.7) were white, polycrystalline aggregates (crystals $\sim 5 \mu\text{m}$), and were either phase pure within the detection limits of XRD or contained traces ($< 2 \text{ wt\%}$) of Al_2O_3 . The lattice parameters and site occupancies determined by Rietveld refinement of the XRD data are given in Table 1. This includes new data for samples (0.44, 0.0) and (0.98, 0.0) for which the structures have been determined previously using NPD data (Doyle et al., 2014). The dependencies of the c lattice parameter and unit cell volume on Ti content for these samples, and determined by NPD (Doyle et al., 2014) and X-ray single-crystal diffraction (Giannini et al., 2014) for samples with a range of $\text{Ti}^{3+}/\Sigma\text{Ti}$ values, are shown in Fig. 1. The a lattice parameter (not plotted) exhibits a similarly good correlation with Ti pfu. Ti was found to only occupy the M2 and M4 sites in agreement with previous studies (Doyle et al., 2014; Giannini et al., 2014). There is one M2 site, which is split into two symmetrically equivalent half-occupied sites by the static displacement of the M2 cation from the site-centre, and two M4 sites pfu. Therefore, Ti pfu due to M2 and M4 is equal to twice the occupancy (as presented in Table 1) and M2/M4 in terms of occupancy is equivalent to M2/M4 in pfu. The Ti^{4+} M4 site occupancy was either determined directly (for samples in which all Ti is assumed to be Ti^{4+}) or calculated by assuming that the total Ti^{4+} pfu is equal to Mg^{2+} pfu and all Ti on M2 is Ti^{4+} (Doyle et al., 2014). Ti^{4+} on the M4 site pfu and the Ti^{4+} M2/M4 site occupancy ratio, as a function of Ti^{4+} pfu, are shown in Fig. 2.

All the hibonite-melt samples were blue. BSE images and elemental maps for representative samples are shown in Fig. 3. The BSE images of all samples show two types of euhedral crystals: blocky crystals (5–15 μm), which often exhibit hexagonal symmetry and are clearly zoned (rims $\sim 1 \mu\text{m}$), and elongate or lath-like crystals (3–5 μm). The lathes and the rims of the zoned crystals are similar in the BSE images and are enriched in Ti and Mg relative to the cores (Fig. 3b). The correlation between the BSE images and the elemental maps suggests that the zoning is real and not an edge effect. The elemental maps also show that hibonite crystals that were originally Mg-free ($\text{CaAl}_{12-y}\text{Ti}^{3+}_y\text{O}_{19}$) contain significant Mg after equilibration with the melt; the distribution of Al distinguishes hibonite from melt (Fig. 3d), Ti is enriched in the crystals relative to what was initially a Ti-free melt (Fig. 3e), and Mg is almost uniformly distributed between hibonite and melt (Fig. 3f). The compositions of the crystals determined by EPMA are given in Table 2. The size of the crystals makes it difficult to obtain analyses that do not contain a contribution from the surrounding quenched melt. In many cases analyses were obtained for a series of points traversing a crystal in the hope of identifying a point for which the melt contribution was minimal. The Si content was used as an indicator of melt since hibonite contains a small or negligible amount (Beckett and Stolper, 1994) whereas the melt contains over 20 wt% SiO_2 . An example traverse is shown in Fig. 4 where the Si content reaches a minimum value in the centre of a crystal. For many samples it

Table 2

Compositions of hibonite crystals, expressed as wt% oxide (± 0.02) and cations per formula unit (± 0.01) for 19 oxygens, after equilibration of $\text{CaAl}_{12-y}\text{Ti}^{3+}_y\text{O}_{19}$ ($\text{Ti}^{3+}/\Sigma\text{Ti} = 1$) hibonite with melt composition A or B at various values of $\log f_{\text{O}_2}$ relative to the IW buffer. $\text{Ti}^{3+}/\Sigma\text{Ti}$ was calculated from stoichiometry assuming $\text{Ti}^{4+} = \text{Mg}$ and $\text{Ti}^{4+} + \text{Si} = \text{Mg}$. For some experiments two different hibonite compositions were identified.

Hibonite	Melt	ΔIW	CaO	Al_2O_3	MgO	TiO_2	SiO_2	Total	Ca	Al	Mg	Ti	Si	Total	$\text{Ti}^{3+}/\Sigma\text{Ti}$ $\text{Ti}^{4+} = \text{Mg}$	$\text{Ti}^{3+}/\Sigma\text{Ti}$ $\text{Ti}^{4+} + \text{Si} = \text{Mg}$
(0.30, 1.0)	A	−0.3	9.45	82.98	1.66	3.60	0.96	98.64	1.15	11.15	0.28	0.31	0.11	13.01	0.09 (5)	0.44 (6)
(0.30, 1.0)	A	−1.3	8.69	84.15	1.80	3.72	0.34	98.71	1.06	11.28	0.31	0.32	0.04	13.00	0.04 (4)	0.16 (5)
(0.30, 1.0)	B	−1.3	8.87	86.18	1.38	2.78	0.29	99.51	1.07	11.44	0.23	0.24	0.03	13.01	0.02 (6)	0.15 (7)
(0.30, 1.0)	A	−2.3	8.83	84.12	1.77	3.87	0.32	98.91	1.07	11.26	0.30	0.33	0.04	13.00	0.09 (4)	0.20 (5)
(0.25, 1.0)	B	−2.3	9.06	87.17	0.65	1.03	0.54	98.46	1.10	11.66	0.11	0.09	0.06	13.02	0.00 (16)	0.45 (20)
(0.15, 1.0)	A	−3.3	9.20	85.78	1.34	2.80	0.46	99.58	1.11	11.39	0.23	0.24	0.05	13.02	0.05 (6)	0.27 (7)
(0.15, 1.0)	A	−3.3	9.02	85.46	1.50	3.36	0.47	99.82	1.09	11.33	0.25	0.28	0.05	13.00	0.12 (5)	0.30 (6)
(0.15, 1.0)	B	−3.3	8.93	88.60	0.67	1.36	0.14	99.70	1.07	11.70	0.11	0.11	0.02	13.02	0.02 (10)	0.16 (15)
(0.15, 1.0)	B	−3.3	8.79	84.32	1.66	3.64	0.23	98.63	1.07	11.31	0.28	0.31	0.03	13.01	0.10 (5)	0.18 (5)
(0.30, 1.0)	A	−3.3	9.21	88.31	0.64	1.24	0.37	99.77	1.11	11.66	0.11	0.10	0.04	13.02	0.00 (12)	0.37 (17)
(0.30, 1.0)	A	−4.3	8.81	85.35	1.54	3.46	0.23	99.38	1.07	11.36	0.26	0.29	0.03	13.00	0.12 (5)	0.21 (6)
(0.15, 1.0)	A	−6.3	9.17	87.98	0.54	1.32	0.15	99.16	1.11	11.70	0.09	0.11	0.02	13.02	0.19 (13)	0.34 (15)
(0.15, 1.0)	A	−6.3	9.03	85.99	1.24	2.92	0.28	99.47	1.09	11.43	0.21	0.25	0.03	13.01	0.16 (6)	0.29 (7)
(0.15, 1.0)	B	−6.3	9.32	87.72	0.89	1.65	0.69	100.27	1.11	11.54	0.15	0.14	0.08	13.02	0.00 (10)	0.49 (13)
(0.25, 1.0)	A	−6.3	9.01	83.56	1.76	4.33	0.34	99.01	1.10	11.19	0.30	0.37	0.04	13.00	0.19 (4)	0.30 (5)
(0.25, 1.0)	A	−6.3	8.95	85.52	1.07	2.85	0.41	98.80	1.09	11.43	0.18	0.24	0.05	12.99	0.26 (6)	0.45 (7)

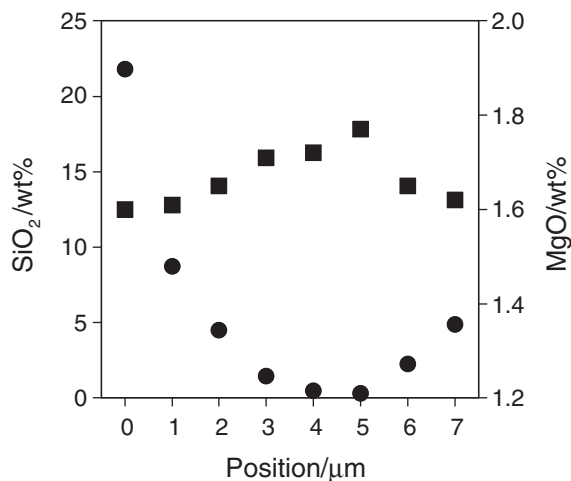


Fig. 4. Variations of SiO_2 (circles) and MgO (squares) determined by EPMA as a function of distance from the edge to centre of a crystal of hibonite in glass for sample (0.30, 1.0) equilibrated with melt A at $\text{IW} - 2.3$. The values at Position = 5 μm are reported in Table 2.

Table 3

Lattice parameters of hibonite and the proportion of phases (wt%), determined by Rietveld QPA refinement, obtained after equilibrating three hibonite compositions at 1400 °C and various values of $\log f_{\text{O}_2}$ relative to the IW buffer.

Composition	ΔIW	a (Å)	c (Å)	Volume (Å ³)	Hibonite	CaTiO_3	MgAl_2O_4	Al_2O_3	Al_2TiO_5	TiO	TiO_2
(0.33, 1.0)	−6.3	5.56676 (6)	21.9471 (3)	589.00 (2)	98.9 (4)	—	—	—	—	1.1 (1)	—
	−2.3	5.56448 (5)	21.9363 (4)	588.23 (1)	61.5 (3)	5.5 (1)	—	32.0 (2)	1.0 (1)	—	—
	−0.3	5.56566 (5)	21.9384 (4)	588.53 (1)	51.0 (3)	6.0 (1)	—	42.0 (2)	1.0 (1)	—	—
	2.3	5.56417 (5)	21.9330 (4)	588.07 (1)	49.1 (3)	6.3 (1)	—	43.2 (2)	1.4 (1)	—	—
	4.3	5.56476 (6)	21.9348 (5)	588.24 (1)	48.2 (3)	6.2 (1)	—	43.9 (2)	1.7 (1)	—	—
	7.3	5.56472 (5)	21.9345 (4)	588.23 (1)	51.0 (3)	6.3 (1)	—	41.3 (2)	1.4 (1)	—	—
(0.62, 0.6)	−6.3	5.57720 (4)	21.9850 (3)	592.23 (1)	93.8 (4)	0.9 (1)	—	4.9 (1)	—	0.4 (1)	—
	−2.3	5.57725 (3)	21.9686 (3)	591.80 (1)	97.0 (3)	3.0 (1)	—	—	—	—	—
	−0.3	5.57634 (3)	21.9609 (3)	591.40 (1)	95.5 (4)	0.6 (1)	—	—	3.9 (1)	—	—
	2.3	5.57527 (3)	21.9614 (3)	591.18 (1)	97.1 (3)	—	—	—	2.9 (1)	—	—
	4.3	5.57470 (3)	21.9561 (2)	590.92 (1)	95.7 (3)	—	—	—	4.3 (1)	—	—
	7.3	5.57511 (3)	21.9616 (3)	591.15 (1)	97.9 (3)	—	—	—	2.1 (1)	—	—
(0.98, 0.0)	−6.3	5.60052 (8)	22.0532 (7)	599.04 (4)	87.1 (4)	3.1 (1)	8.8 (1)	—	—	—	1.0 (1)
	−2.3	5.60843 (6)	22.0745 (5)	601.32 (1)	93.0 (4)	2.1 (1)	4.5 (1)	0.4 (1)	—	—	—
	2.3	5.60949 (4)	22.0843 (4)	601.81 (1)	96.1 (4)	1.4 (1)	2.0 (1)	—	0.5 (1)	—	—
	4.3	5.60959 (3)	22.0843 (5)	601.83 (1)	97.2 (3)	1.1 (1)	1.7 (1)	—	—	—	—
	7.3	5.60886 (4)	22.0856 (4)	601.71 (1)	96.0 (3)	1.7 (1)	2.3 (1)	—	—	—	—

was not possible to obtain analyses of hibonite that were not contaminated by the melt and only the analysis with the lowest SiO_2 value, if also < 1.0 wt% (average ~0.4 wt%), is reported in Table 2. Thus, these results are for the subset of samples for which the analyses are considered reliable. For some samples two different hibonite compositions were obtained and both are given in Table 2. The SiO_2 contents are consistent with values reported previously for hibonite (Beckett and Stolper, 1994; Simon et al., 1997), but if they were to arise from the surrounding melt the associated contribution to the Mg and Ti contents of the hibonite would be < 0.1 wt%. The independence of the Si and Mg concentrations shown in Fig. 4 indicates that the Mg in the crystal is not an artefact attributable to the melt.

The oxide compositions corresponding to (0.98, 0.0), (0.62, 0.6), and (0.33, 1.0) produced polycrystalline hibonite at 1400 °C and all values of f_{O_2} ($\text{IW} - 6.3$ to $\text{IW} + 7.3$), plus varying amounts of CaTiO_3 , MgAl_2O_4 , Al_2O_3 , Al_2TiO_5 , and Ti-oxides. The hibonite lattice parameters and the phase proportions of each sample are given in Table 3, and the variations of the c lattice parameter and wt% of hibonite as a function of f_{O_2} are shown in Fig. 5. It is not possible to distinguish Mg from Al using XRD data and hence site occupancies and $\text{Ti}^{3+}/\Sigma\text{Ti}$ could not be determined for these samples. The powdered products were a shade of blue for all three compositions at f_{O_2} s equal to and below IW

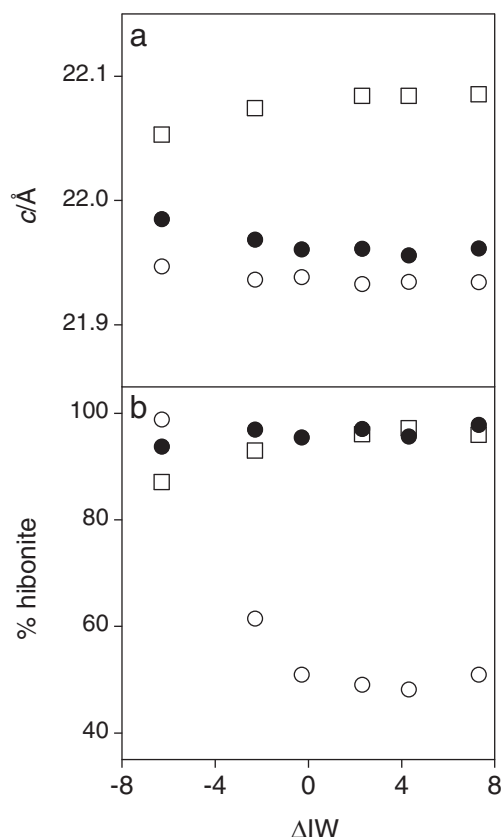


Fig. 5. (a) c lattice parameter of hibonite and (b) wt% hibonite determined by QPA of samples obtained by equilibrating oxides corresponding to the hibonite compositions (0.98, 0.0) (open squares), (0.62, 0.6) (solid circles) and (0.33, 1.0) (open circles) at 1400 °C and various values of $\log fO_2$ relative to the IW buffer. Error bars are smaller than the symbols.

+4.3, while the product of composition (0.62, 0.6) was also blue at IW +7.3.

Ti K-edge XANES spectra recorded from different points on each $CaAl_{12-2x}Mg_xTi^{4+}_xO_{19}$ sample were essentially identical. Spectra recorded from a randomly oriented single crystal as a function of orientation to the X-ray beam were also essentially identical (Doyle et al., 2016). Spectra for samples (0.1, 0.0) and (0.44, 0.0) are shown in Fig. 6(b, d). Also shown are spectra for two hibonite crystals from the Murchison carbonaceous chondrite (10-43 and 7-981), which are typical of two spectral types that were observed for a number of crystal fragments. Sample 10-43 (Blue AGgregate or BAG) contains 6.44 wt% TiO_2 (0.55 Ti pfu) and has the formula $Ca_{1.03}Al_{10.93}Mg_{0.48}Ti_{0.55}O_{19}$, while 7-981 (PLAty Crystal or PLAC) contains 1.19 wt% TiO_2 (0.1 Ti pfu) and corresponds to $Ca_{1.01}Al_{11.78}Mg_{0.12}Ti_{0.10}O_{19}$ (Ireland, 1988). The pre-edge region for these two samples, for synthetic samples with $Ti^{3+}/\Sigma Ti = 0$ but varying Ti pfu, and a synthetic sample with $Ti^{3+}/\Sigma Ti = 1$ (Doyle et al., 2016) are shown in Fig. 7. Spectra of other Murchison crystals, and hibonite in CAIs from various R3, CR2, and unique meteorites will be presented elsewhere.

Ti K-edge XANES spectra for hibonite with Ti^{3+} and Ti^{4+} at various substitutional sites, modelled using FDMNES, are shown in Fig. 8. The pre-edge regions of the Ti^{4+} models are shown in Fig. 9 along with the spectrum of sample 10-43. In both figures the spectrum resulting from a linear combination of the spectra for Ti^{4+} on M2 and Ti^{4+} clustered on M4, in a proportion similar to that predicted by XRD and NPD for hibonite with a Ti pfu comparable to that of 10-43, is also shown.

4. Discussion

Hibonite containing only Ti^{4+} is colourless (appears white), that containing only Ti^{3+} is grey or blue, while mixed valent samples containing both Ti^{3+} and Ti^{4+} are deep blue. The blue colour arises from the d^1 electronic configuration of Ti^{3+} and may correspond to either a $d-d$ transition or charge transfer between Ti^{3+} and Ti^{4+} , noting that such an interaction has been reported for Ti in Al_2O_3 (Yamaga et al., 1994) and that Ti^{3+} and Ti^{4+} may occupy neighbouring, face-sharing M4 octahedra in hibonite. The colour blue is considered to be diagnostic of hibonite in CAIs (Ireland, 1988) and the presence of Ti^{3+} is generally taken to imply that crystals formed or equilibrated under reduced conditions.

$Ti^{3+}/\Sigma Ti$ in a melt will have a sigmoidal dependence on fO_2 (see Berry and O'Neill, 2004). If hibonite crystallises from a condensate (a low density melt) then $Ti^{3+}/\Sigma Ti$ in hibonite should be related to $Ti^{3+}/\Sigma Ti$ in the condensate. However, the partition coefficients of Ti^{3+} and Ti^{4+} will be different and the uptake of Ti^{4+} will depend on the availability of Mg (for charge balance). In the absence of Mg all Ti in hibonite must be Ti^{3+} (i.e. $Ti^{3+}/\Sigma Ti = 1$), irrespective of the fO_2 , and the amount of Ti will depend on the activity of Ti^{3+} in the condensate or melt. In the synthesis of mixed-valent samples from oxides a range of $Ti^{3+}/\Sigma Ti$ values (= 0.27, 0.33, 0.39, 0.60, and 1.0) were all prepared at constant fO_2 (IW – 6.3) by varying the amount of Mg (Doyle et al., 2014). The Mg pfu required a stoichiometric amount of Ti to be Ti^{4+} with any Ti pfu > Mg pfu attributed to Ti^{3+} . Determining $Ti^{3+}/\Sigma Ti$ in these samples would thus provide no insight into the fO_2 of formation.

The role of crystal chemistry was investigated further in this study by the experiments in which oxide compositions corresponding to hibonites containing only Ti^{3+} , only Ti^{4+} , and both Ti^{3+} and Ti^{4+} were heated at 1400 °C and values of fO_2 corresponding to IW – 6.3 to +7.3. For each composition the lattice parameters of the hibonite were similar at all fO_2 s (Fig. 5a), despite the sensitivity of the parameters to ΣTi (Fig. 1) and Ti^{4+} pfu (Doyle et al., 2014). Although the Ti^{3+} composition yielded a large proportion of impurity phases at all fO_2 s other than the most reduced, hibonite was always the dominant phase for the other two compositions (Fig. 5b; Table 3). Indeed, the mixed valent composition produced almost phase pure hibonite over the entire fO_2 range with very little change in the lattice parameter i.e. hibonite with $Ti^{3+}/\Sigma Ti \sim 0.6$ was prepared over 13 log units in fO_2 . This suggests that crystal chemistry stabilises Ti^{3+} and Ti^{4+} to significantly more oxidised and reduced conditions, respectively, than might be expected. Thus, a range of $Ti^{3+}/\Sigma Ti$ values can be produced at a single fO_2 and a constant $Ti^{3+}/\Sigma Ti$ value can be produced for a range of fO_2 s.

Melt composition A at 1450 °C should produce hibonite and melt (Beckett and Stolper, 1994). Therefore, the equilibration experiments between hibonite and melt A might be expected to yield two generations of hibonite: the pre-synthesised starting material after equilibration with the melt and liquidus crystals. Melt composition B (Ti-free) was chosen to suppress the formation of liquidus hibonite. The large blocky crystals are attributed to the pre-synthesised hibonite and the small lathe-like crystals and rims on the blocky crystals to hibonite that crystallised from the melt, either at the experimental conditions or on quenching. All experiments produced both generations of hibonite, including those with melt B, indicating that the pre-synthesised hibonite partially dissolved in melt B to produce a modified melt that crystallised new hibonite. This is consistent with the presence of Ti in the quenched melts. The composition of the pre-synthesised hibonite was of the form $CaAl_{12-y}Ti^{3+}_yO_{19}$, yet all the hibonite analyses in Table 2 contain Mg in an amount approximately equal to that of Ti, in pfu. The Mg, as illustrated in Fig. 4, is unambiguously present in the hibonite and cannot be attributed to fluorescence derived from the surrounding melt. The presence of Mg, seemingly homogeneously distributed in the crystals, is shown in Fig. 3f. For some samples different hibonite compositions are reported in Table 2 and these are attributed to the re-equilibrated and liquidus crystals, however, all have

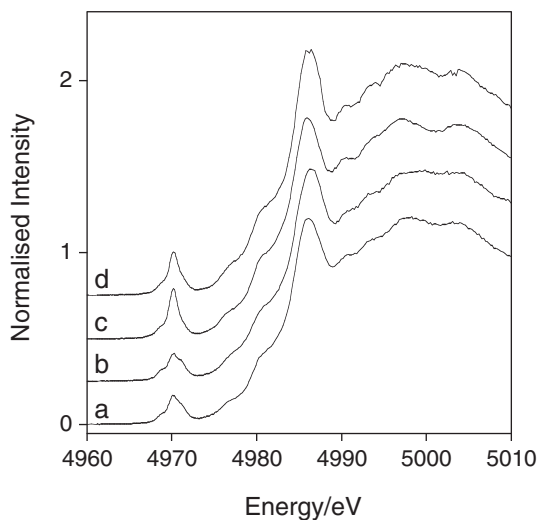


Fig. 6. Ti K-edge XANES spectra of natural hibonite samples (a) 10-43 (0.55 Ti pfu) and (c) 7-981 (0.1 Ti pfu) from the Murchison carbonaceous chondrite, and synthetic hibonite with compositions (b) (0.44, 0.0) and (d) (0.1, 0.0). Spectra are offset for clarity.

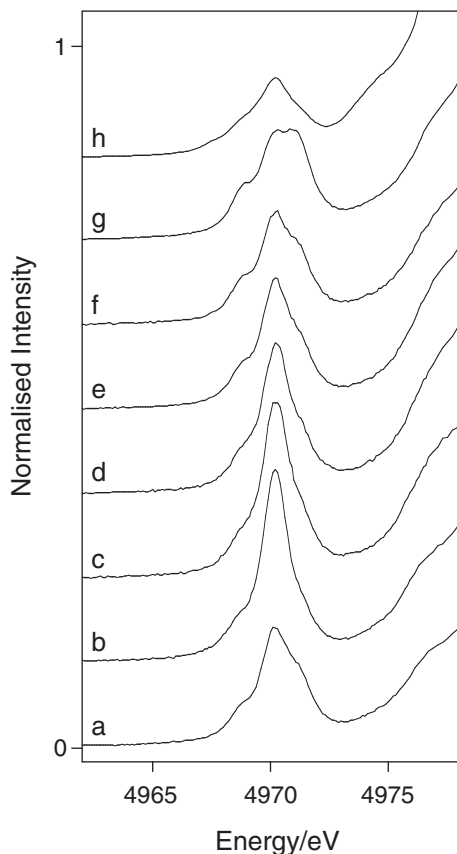


Fig. 7. The pre-edge region of Ti K-edge XANES spectra of natural hibonite samples (a) 10-43 (0.55 Ti pfu) and (b) 7-981 (0.1 Ti pfu) from the Murchison carbonaceous chondrite, and synthetic hibonite with compositions (c) (0.1, 0.0), (d) (0.2, 0.0), (e) (0.3, 0.0), (f) (0.44, 0.0), (g) (0.98, 0.0), and (h) (0.2, 1.0). Spectra are offset for clarity.

Ti pfu \sim Mg pfu. The Ti pfu in some cases corresponds closely to that of the pre-synthesised hibonite. In other cases the crystal analysed could have grown from the melt or represent a composition closer to crystal-melt equilibrium. The key point is hibonite crystals that contained Ti only as Ti^{3+} have incorporated Mg during equilibration with a melt and as a result now contain Ti as predominantly Ti^{4+} , at all $f\text{O}_2$ s. The

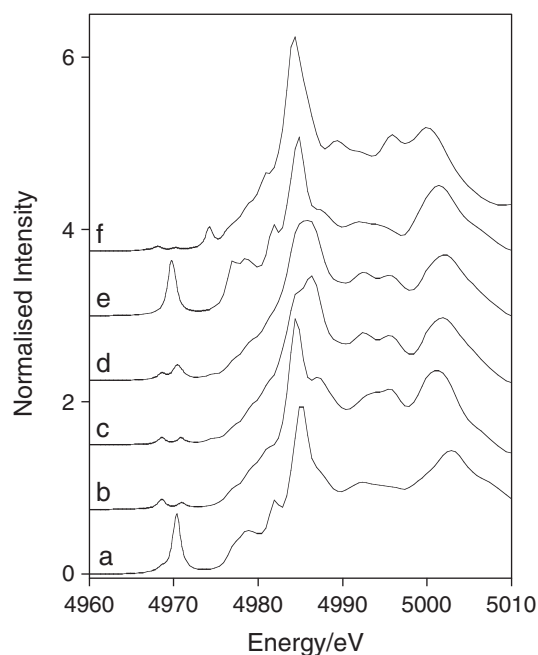


Fig. 8. Simulated Ti K-edge XANES spectra of hibonite, modelled using FDMNES, with (a) Ti^{4+} on M2, (b) Ti^{4+} on M4, (c) Ti^{4+} clustered on adjacent M4, (d) Ti^{4+} on M2 (20%) and Ti^{4+} clustered on adjacent M4 (80%), (e) Ti^{3+} on M2, and (f) Ti^{3+} clustered on adjacent M4. Spectra are offset for clarity.

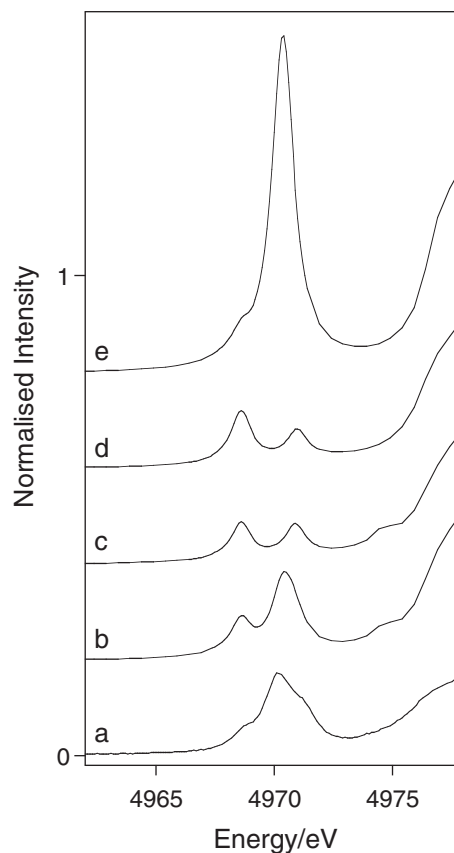


Fig. 9. The pre-edge region of the Ti K-edge XANES spectrum of (a) natural hibonite sample 10-43, and simulated spectra, modelled using FDMNES, of hibonite with (b) Ti^{4+} on M2 (20%) and Ti^{4+} clustered on adjacent M4 (80%), (c) Ti^{4+} clustered on adjacent M4, (d) Ti^{4+} on M4, and (e) Ti^{4+} on M2. Spectra are offset for clarity.

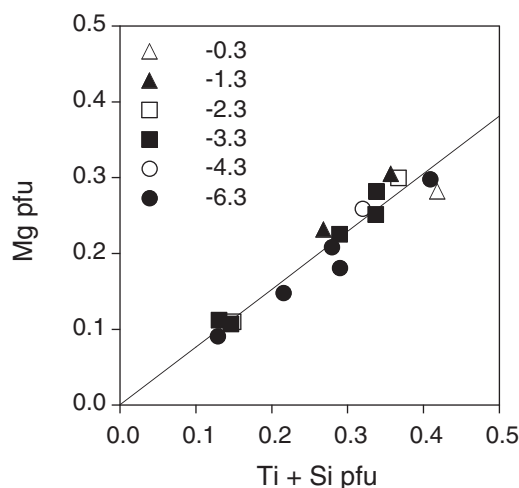


Fig. 10. Correlation between Mg and Ti + Si pfu for hibonite crystals equilibrated in a CAI composition melt at 1450 °C and the values of fO_2 , in log units relative to the IW buffer, indicated. The line is the best fit to the data and has a slope of ~ 0.8 .

average value of $Ti^{3+}/\Sigma Ti$ calculated from stoichiometry is 0.09(8), assuming Ti^{4+} pfu = Mg pfu, or 0.30(11) if $Ti^{4+} + Si$ pfu = Mg pfu (Mg^{2+} may be charge balanced by both Ti^{4+} and Si^{4+} ; Simon et al., 1997). The correlation between Mg and Ti + Si pfu is shown in Fig. 10 and has a slope of ~ 0.8 . If Ti pfu is converted to Ti^{4+} pfu using the average value of $Ti^{3+}/\Sigma Ti$ then the slope of the correlation is ~ 1 . The ratio of Mg to Ti + Si is constant and independent of fO_2 . The correlation between Mg and Ti also has a slope of ~ 0.8 but does not pass through 0 (intercept 0.02). Equilibration of hibonite with a melt of CAI composition results in the uptake of Mg and, for charge balance, a stoichiometric amount of Ti^{3+} must be oxidised to Ti^{4+} , even at IW – 6.3. This suggests that the Mg activity of the melt, and hence crystal chemistry, is more important for determining the $Ti^{3+}/\Sigma Ti$ value of hibonite than fO_2 . These experiments were designed to simulate the equilibration of crystallised/condensed hibonite with further condensate or melt and it is noted that the $Ti^{3+}/\Sigma Ti$ values obtained are similar to those estimated for hibonite from the Murchison carbonaceous chondrite (0.15–0.28; Beckett et al., 1988).

The condensation temperatures of the major elements, for a gas of solar composition at a pressure of < 0.01 atm., decrease in the order Al, Ca, Ti, Si, Mg, Fe (Lodders, 2003). Corundum is the first phase to condense (Yoneda and Grossman, 1995) and may contain up to 0.25 wt % Ti (Simon et al., 2002), most likely as Ti^{3+} . With continued cooling and condensation corundum is believed to react with Ca to form hibonite. Accordingly, corundum-bearing CAIs are rare and corundum has been found enclosed by hibonite (Simon et al., 2002; Nakamura et al., 2007). The first meteoritic hibonite to condense might be expected to have the composition $CaAl_{12-y}Ti_yO_{19}$. Further condensation would make Mg available to the system. If Mg was to equilibrate with hibonite, which at that point would contain Ti as only Ti^{3+} , then Ti^{3+} must oxidise to Ti^{4+} in order for the Mg to be accommodated. If new hibonite that contains Mg was to crystallise then it must also contain Ti^{4+} . The addition of Mg and Ti from a melt to early-formed meteoritic hibonite has been proposed as a mechanism for producing rims of secondary hibonite with different Mg:Ti ratios and colours (Simon et al., 1997). Meteoritic hibonite with small blue cores surrounded by thick colourless rims has been observed (Rout and Bischoff, 2008). The difference in colour was attributed to differences in the Ti content but could also be due to differences in Mg content and hence Ti oxidation state, noting a strong 1:1 correlation between Mg pfu and Ti pfu overall but $Ti > Mg$ for the blue components. This 1:1 correlation, which is a general characteristic of meteoritic hibonite (see Doyle et al., 2014), the ability to synthesise hibonite under reduced conditions with almost any $Ti^{3+}/\Sigma Ti$ depending on the available Mg, and the fact that hibonite

with $Ti^{3+}/\Sigma Ti = 1$ will gain Mg during equilibration with a CAI melt composition resulting in $Ti^{3+}/\Sigma Ti \sim 0.2$, independently of fO_2 (at least below IW), indicate that stoichiometry, or the activity of Mg, is more important for controlling $Ti^{3+}/\Sigma Ti$ than fO_2 .

The lattice parameters and unit cell volumes determined by X-ray powder diffraction (Table 1) are consistent with those of other studies (Fig. 1). The increase with Ti pfu is mainly due to the corresponding increase in Mg pfu and the larger size of Mg^{2+} relative to Al^{3+} (Doyle et al., 2014). XRD provides excellent contrast between Al and Ti and the occupancies of Ti^{4+} on M4 (Fig. 2a) as a function of Ti^{4+} pfu are similar to those determined by NPD and single-crystal XRD (Doyle et al., 2014; Giannini et al., 2014). The slope of the correlation is < 1 (~ 0.8) because Ti^{4+} also occupies the M2 site. The ratio of the Ti^{4+} occupancy of M2 and M4 (Fig. 2b) determined in this study varies systematically with Ti^{4+} pfu. At low concentrations Ti^{4+} predominantly occupies the M2 site, as predicted by DFT for isolated cations, while at higher concentrations Ti^{4+} prefers the M4 site due to the stabilising Ti–Ti interaction that occurs if adjacent M4 sites are occupied (Doyle et al., 2014). All the data are in general agreement with the trend, although the mixed-valent sample with the highest value of $Ti^{3+}/\Sigma Ti$ (0.62, 0.60) has an unexpectedly low Ti^{4+} M2/M4 value, which may indicate a stabilising $Ti^{3+}(M4)-Ti^{4+}(M4)$ interaction that results in Ti^{4+} occupying M4 even at low Ti^{4+} pfu.

The Ti K-edge XANES spectra of the (0.1, 0.0) and (0.44, 0.0) synthetic samples are very similar (pre-edge, edge, and post-edge) to those of natural samples 7–981 (0.1 Ti pfu) and 10–43 (0.55 Ti pfu), respectively (Fig. 6). This is shown in more detail for the pre-edge in Fig. 7. For the samples with $Ti^{3+}/\Sigma Ti = 0$ the pre-edge systematically decreases in maximum intensity and broadens (develops shoulders at lower and higher energies) with increasing Ti^{4+} pfu (from ~ 0.1 to 1.0). Over this range Ti^{4+} changes site from M2 to predominantly M4. The pre-edge feature corresponds to the $1s \rightarrow 3d$ transition, which is forbidden in octahedral coordination, but may gain intensity by orbital mixing in lower symmetry environments. Accordingly, for Ti^{4+} , the pre-edge intensity has been shown to increase from $[^{6}Ti]$ to $[^{5}Ti]$ to $[^{4}Ti]$ coordination (Farges et al., 1996). In hibonite a change in site symmetry from trigonal bipyramidal ($[^{5}M2]$) to octahedral ($[^{6}M4]$) should therefore be associated with a decrease in pre-edge intensity, as observed. The pre-edge region of 7–981 is consistent with most of the Ti^{4+} occupying the M2 site (compare b and c in Fig. 7) and that of 10–43 with Ti^{4+} occupying both M2 and M4 (compare a and f in Fig. 7). The effect of what would be a small (from stoichiometry) amount of Ti^{3+} in 10–43 on the pre-edge is insignificant given the shape of the pre-edge for (0.2, 1.0) shown in Fig. 7h. Changes in Ti^{4+} site occupancy with changes in concentration, at constant fO_2 , produce changes in the XANES spectra that could easily be misinterpreted as being due to changes in $Ti^{3+}/\Sigma Ti$. The XANES spectra of meteoritic hibonite differ with ΣTi , which relates to the petrogenetic history, and the effect of differences in Ti site occupancy will be convolved with any differences in $Ti^{3+}/\Sigma Ti$.

The large effect of the Ti^{4+} site occupancy on the pre-edge is confirmed by the XANES models shown in Fig. 9. The pre-edge for Ti^{4+} on M2 is significantly more intense, and less structured than that for Ti^{4+} on M4, either as an isolated cation or as a cluster. The Ti^{4+} site occupancy of sample 10–43 is expected to be around 20% M2 and 80% M4 and the simulated spectrum for this occupancy is in reasonable agreement with what is observed (compare a and b in Fig. 9). The agreement between the simulated and experimental spectra for the edge and post-edge regions (Figs. 6 and 8) is less good but not unreasonable given the complexity of the models.

To determine $Ti^{3+}/\Sigma Ti$ in hibonite by XANES spectroscopy would require a large set of well-characterised standards. These standards would need to encompass not only variable $Ti^{3+}/\Sigma Ti$ but also different ΣTi to account for changes in the Ti site at constant $Ti^{3+}/\Sigma Ti$ and the diversity of possible Ti–Ti interactions ($Ti^{3+}-Ti^{3+}$, $Ti^{4+}-Ti^{4+}$, $Ti^{3+}-Ti^{4+}$) across the shared face of the M4 octahedra. Standards may be

characterised by determining ΣTi and Mg by EPMA and estimating $\text{Ti}^{3+}/\Sigma\text{Ti}$ by assuming $\text{Ti}^{4+} = \text{Mg}^{2+}$. EPMA may similarly be used to evaluate $\text{Ti}^{3+}/\Sigma\text{Ti}$ of meteoritic hibonite if the amount of Si is determined accurately (Simon et al., 1997), although the presence of relatively small amounts of other transition metals may introduce significant uncertainties.

We have shown that hibonite with almost any value of $\text{Ti}^{3+}/\Sigma\text{Ti}$ can be prepared at constant $f\text{O}_2$ and that a constant value of $\text{Ti}^{3+}/\Sigma\text{Ti}$ can be produced over a range of $f\text{O}_2$. Hibonite will equilibrate with a melt that contains Mg to produce a $\text{Ti}^{3+}/\Sigma\text{Ti}$ value that is independent of $f\text{O}_2$. Meteoritic hibonite may re-equilibrate with post-formation conditions by changing its Mg content and hence $\text{Ti}^{3+}/\Sigma\text{Ti}$ value. The primary factor that controls the $\text{Ti}^{3+}/\Sigma\text{Ti}$ ratio is the availability of Mg rather than $f\text{O}_2$. The crystal chemistry also determines the Ti site occupancy, which varies with Ti concentration. The site occupied by Ti clearly affects the XANES spectrum and the potential for it to be used to determine $\text{Ti}^{3+}/\Sigma\text{Ti}$. Changes in site occupancy and the resulting Ti-Ti interactions will similarly affect other spectroscopic techniques, such as optical absorption, ESR, XPEEM, STXM and electron energy loss (EELS). The crystal chemistry of hibonite severely compromises its ability to record a $\text{Ti}^{3+}/\Sigma\text{Ti}$ value that relates to $f\text{O}_2$ or for $\text{Ti}^{3+}/\Sigma\text{Ti}$ to be quantified accurately.

Acknowledgements

We thank Dean Scott for preparing some of the samples, John Spratt for assistance with the electron microprobe analyses, Jens Najorka for recording some of the XRD patterns, Patricia Doyle for helping to acquire the XANES spectra of 10-43 and 7-981, and Diamond Light Source for providing beamtime. A.J.B. thanks the Australian Research Council for a Future Fellowship, A.N.K. and A.V.S. thank the Ministry of Education and Science of the Russian Federation for the award of grant 16.3871.2017/ПЧ ("Picometre diagnostics of parameters of 3D atomic structure of nanomaterials on the basis of XANES spectroscopy"), and A.M.W. thanks the Natural Environment Research Council for an Independent Research Fellowship (NE/K008803/1). Steven Simon is thanked for his review of the manuscript.

References

- Beckett, J.R., Stolper, E., 1994. The stability of hibonite, melilite and other aluminous phases in silicate melts: implications for the origin of hibonite-bearing inclusions from carbonaceous chondrites. *Meteoritics* 29, 41–65.
- Beckett, J.R., Live, D., Tsay, F.-D., Grossman, L., Stolper, E., 1988. Ti^{3+} in meteoritic and synthetic hibonite. *Geochim. Cosmochim. Acta* 52, 1479–1495.
- Berry, A.J., O'Neill, H.St.C., 2004. A XANES determination of the oxidation state of chromium in silicate glasses. *Am. Mineral.* 89, 790–798.
- Berry, A.J., Walker, A.M., Hermann, J., O'Neill, H.St.C., Foran, G.J., Gale, J.D., 2007. Titanium substitution mechanisms in forsterite. *Chem. Geol.* 242, 176–186.
- Berry, A.J., Danyushevsky, L.V., O'Neill, H.St.C., Newville, M., Sutton, S.R., 2008. The oxidation state of iron in komatiitic melt inclusions indicates hot Archaean mantle. *Nature* 455, 960–963.
- Berry, A.J., Yaxley, G.M., Woodland, A.B., Foran, G.J., 2010. A XANES calibration for determining the oxidation state of iron in mantle garnet. *Chem. Geol.* 278, 31–37.
- Bunau, O., Joly, Y., 2009. Self-consistent aspects of X-ray absorption calculations. *J. Phys. Condens. Matter* 21, 345501.
- Burnham, A.D., Berry, A.J., Halse, H.R., Schofield, P.F., Cibir, G., Mosselmans, J.F.W., 2015. The oxidation state of europium in silicate melts as a function of oxygen fugacity, composition and temperature. *Chem. Geol.* 411, 248–259.
- Doyle, P.M., Schofield, P.F., Berry, A.J., Walker, A.M., Knight, K.S., 2014. Substitution of Ti^{3+} and Ti^{4+} in hibonite (CaAl_2O_6). *Am. Mineral.* 99, 1369–1382.
- Doyle, P.M., Berry, A.J., Schofield, P.F., Mosselmans, J.F.W., 2016. The effect of site geometry, Ti content and Ti oxidation state on the Ti K-edge XANES spectrum of synthetic hibonite. *Geochim. Cosmochim. Acta* 187, 294–310.
- Farges, F., Brown Jr., G.E., Rehr, J.J., 1996. Coordination chemistry of Ti(IV) in silicate glasses and melts: I. XAFS study of titanium coordination in oxide model compounds. *Geochim. Cosmochim. Acta* 60, 3023–3038.
- Giannini, M., Boffa Ballaran, T., Langenhorst, F., 2014. Crystal chemistry of synthetic Ti-Mg-bearing hibonites: a single-crystal X-ray study. *Am. Mineral.* 99, 2060–2067.
- Ihinger, P.D., Stolper, E., 1986. The color of meteoritic hibonite: an indicator of oxygen fugacity. *Earth Planet. Sci. Lett.* 78, 67–79.
- Ireland, T.R., 1988. Correlated morphological, chemical, and isotopic characteristics of hibonites from the Murchison carbonaceous chondrite. *Geochim. Cosmochim. Acta* 52, 2827–2839.
- Ireland, T.R., 1990. Presolar isotopic and chemical signatures in hibonite-bearing refractory inclusions from the Murchison carbonaceous chondrite. *Geochim. Cosmochim. Acta* 54, 3219–3237.
- Ireland, T.R., Zinner, E.K., Fahey, A.J., Esat, T.M., 1992. Evidence for distillation in the formation of HAL and related hibonite inclusions. *Geochim. Cosmochim. Acta* 56, 2503–2520.
- Jerebtsov, D.A., Mikhailov, G.G., 2001. Phase diagram of $\text{CaO-Al}_2\text{O}_3$ system. *Ceram. Int.* 27, 25–28.
- Joly, Y., 2001. X-ray absorption near edge structure calculations beyond the muffin-tin approximation. *Phys. Rev. B* 63, 125120.
- Kornacki, A.S., Fegley Jr., B., 1986. The abundance and relative volatility of refractory trace elements in Allende Ca,Al-rich inclusions: implications for chemical and physical processes in the solar nebula. *Earth Planet. Sci. Lett.* 79, 217–234.
- Larson, A.C., Von Dreele, R.B., 1994. General Structure Analysis System (GSAS). Los Alamos National Laboratory Report. LAUR 86-748 (revised version).
- Lodders, K., 2003. Solar system abundances and condensation temperatures of the elements. *Astrophys. J.* 591, 1220–1247.
- Mosselmans, J.F., Quinn, P.D., Dent, A.J., Cavill, S.A., Moreno, S.D., Peach, A., Leicester, P.J., Keylock, S.J., Gregory, S.R., Atkinson, K.D., Rosell, J.R., 2009. I18 - the microfocus spectroscopy beamline at the Diamond Light Source. *J. Synchrotron Radiat.* 16, 818–824.
- Nakamura, T.M., Sugiura, N., Kimura, A., Miyazaki, A., Krot, A.N., 2007. Condensation and aggregation of solar corundum and corundum-hibonite grains. *Meteorit. Planet. Sci.* 42, 1249–1265.
- Rout, S., Bischoff, A., 2008. Ca,Al-rich inclusions in Rumuruti (R) chondrites. *Meteorit. Planet. Sci.* 43, 1439–1464.
- Schofield, P.F., Smith, A.D., Scholl, A., Doran, A., Covey-Crump, S.J., Young, A.T., Ohldag, H., 2014. Chemical and oxidation-state imaging of mineralogical intergrowths: the application of X-ray Photo-Emission Electron Microscopy (XPEEM). *Coord. Chem. Rev.* 277–278, 31–43.
- Simon, S.B., Grossman, L., Davis, A.M., 1997. Multiple generations of hibonite in spinel-hibonite inclusions from Murchison. *Meteorit. Planet. Sci.* 32, 259–269.
- Simon, S.B., Davis, A.M., Grossman, L., McKeegan, K.D., 2002. A hibonite-corundum inclusion from Murchison: a first-generation condensate from the solar nebula. *Meteorit. Planet. Sci.* 37, 533–548.
- Simon, S.B., Sutton, S.R., Grossman, L., 2007. Valence of titanium and vanadium in pyroxene in refractory inclusion interiors and rims. *Geochim. Cosmochim. Acta* 71, 3098–3118.
- Tailby, N.D., Walker, A.M., Berry, A.J., Hermann, J., Evans, K.A., Mavrogenes, J.A., O'Neill, H.St.C., Rodina, I.S., Soldatov, A.V., Rubatto, D., Sutton, S.R., 2011. Ti site occupancy in zircon. *Geochim. Cosmochim. Acta* 75, 905–921.
- Toby, B.H., 2001. EXPGUI, a graphical user interface for GSAS. *J. Appl. Crystallogr.* 34, 210–221.
- Yamaga, M., Yosida, T., Hara, S., Kodama, N., Henderson, B., 1994. Optical and electron spin resonance spectroscopy of Ti^{3+} and Ti^{4+} in Al_2O_3 . *J. Appl. Phys.* 75, 1111–1117.
- Yoneda, S., Grossman, L., 1995. Condensation of $\text{CaO-MgO-Al}_2\text{O}_3\text{-SiO}_2$ liquids from cosmic gases. *Geochim. Cosmochim. Acta* 59, 3413–3444.